Supporting information

Morphological impact of 1-dimensional → 3-dimensional manganese dioxides on ozone catalytic decomposition correlated with crystal facet and lattice oxygen mobility

Haotian Wu, Runduo Zhang[*], Bin Kang, Xiaonan Guo, Zhaoying Di, Kun Wang, Jingbo Jia, Ying Wei, Zhou-jun Wang

State Key Laboratory of Chemical Resource Engineering, Beijing Key Laboratory of Energy Environmental Catalysis, Beijing University of Chemical Technology, Beijing 100029, China

[*]Corresponding Author: zhangrd@mail.buct.edu.cn (Runduo Zhang)

Content

S1. Experimental section

1.1 Preparation of MnO$_2$

α-MnO$_2$, β-MnO$_2$, γ-MnO$_2$ and δ-MnO$_2$ were prepared by a hydrothermal method. For α-MnO$_2$, the detailed steps were as follows: 1.00 g of MnSO$_4$·H$_2$O and 2.38 g of KMnO$_4$ were mixed in 150 mL of distilled water, and 3.8 mL of 68% HNO$_3$ was added, and then magnetically stirred for about 1 h to form a homogeneous solution. The mixed solution was then transferred into a Teflon-lined reactor. Afterwards, the reactor was heated in an oven at 100 °C for 24 h and then cooled to room temperature. The resulting product was collected by centrifugation and dried at 80 °C for 12 h to obtain α-MnO$_2$.

The preparation of β-MnO$_2$, γ-MnO$_2$ and δ-MnO$_2$ was similar to that of α-MnO$_2$. The different steps are as follows: for β-MnO$_2$, 1.00 g MnSO$_4$·H$_2$O and 1.35 g (NH$_4$)$_2$S$_2$O$_8$ were mixed, and the reactor was heated at 140 °C for 12 h. For γ-MnO$_2$, 1.00 g MnSO$_4$·H$_2$O and 1.36 g (NH$_4$)$_2$S$_2$O$_8$ were mixed, and the reactor was heated at 90 °C for 24 h. For δ-MnO$_2$, 1.00 g MnSO$_4$·H$_2$O and 5.45 g KMnO$_4$ were mixed and heated at 160 °C for 24 h. The obtained α-MnO$_2$ and β-MnO$_2$ were calcined under N$_2$ atmosphere at 400 °C, γ-MnO$_2$ and δ-MnO$_2$ were calcined at 200 °C and 300 °C, respectively.

For ε-MnO$_2$, the detailed procedure is described below: 1.00 g of MnSO$_4$·H$_2$O and 4.98 g of NaHCO$_3$ were dissolved in 200 mL of distilled water, respectively, and then 5.18 mL of anhydrous ethanol was added dropwise into the MnSO$_4$ solution to form a homogeneous solution, and then NaHCO$_3$ solution was added dropwise into the resulting MnSO$_4$ solution. The mixed solution was magnetically stirred at room temperature for 3 h. After that, the residue was collected by centrifugation, dried at 80 °C for 12 h, and then calcined at 400 °C for 6 h to obtain ε-MnO$_2$.

The hydrothermal tandem calcination method was used to prepare λ-MnO$_2$, and the detailed steps were as follows: 0.21 g of LiAc and 1.00 g of Mn(Ac)$_2$ were added into 15 mL of distilled water, and then 0.8 mL of 68 % HNO$_3$ was added to adjust the pH to 1-3, and then 1.28 g of citric acid was added into the mixed solution. After that, the mixed solution was magnetically stirred at room temperature for 1 h, and then it

was transferred into a Teflon-lined reactor. Afterwards, the reactor was heated to 160 °C in an oven for 24 h and cooled to room temperature. The resulting sol was then stirred in an oil bath at 80 °C to obtain a gel. The obtained gel was dried at 120 °C for 12 h and calcined at 750 °C for 6 h. Finally, the obtained black powder was immersed in 1.2 mol-L^{-1} H_2SO_4 for 12 h. Finally, the obtained product was collected by centrifugation and dried at 80 °C for 12 h to obtain λ-MnO_2. Since the catalytic activity of MnO_2 is sensitive to water vapor (H_2O), all the as-prepared samples of MnO_2 were stored under dry conditions.

According to the stability of different crystalline[S1], the as-prepared sample are Calcined in a tube furnace under N_2 atmosphere for 4 h. The calcination temperature of α-MnO_2 and β-MnO_2 is 400 °C, and the temperature of γ-MnO_2 and δ-MnO_2 is 200 °C.

All the collected MnO_2 samples were stored under dry conditions, owing to the catalytic activity of MnO_2 is sensitive to water (H_2O).
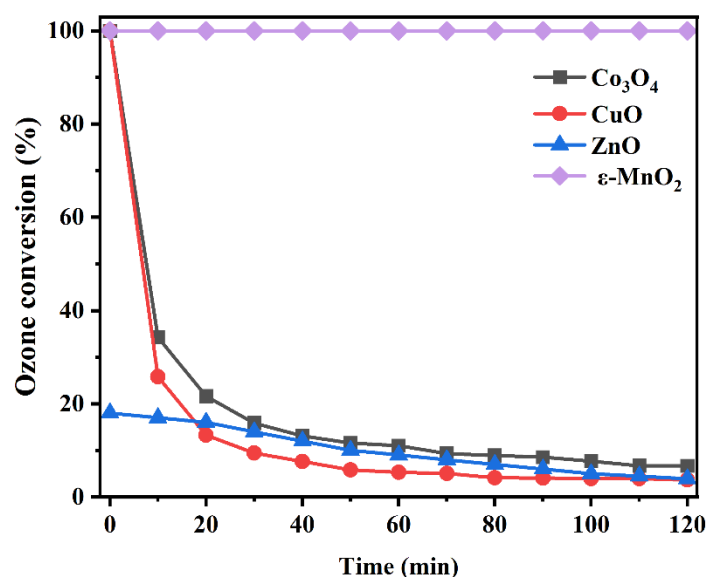

Figure S1 The performance of Co_3O_4, CuO, ZnO and ε-MnO_2 on ozone removal. Conditions:25 °C, 40 ppm, RH = 0, catalyst mass 100 mg, GHSV= 5800 h^{-1}.

1.2 Characterization

X-ray diffraction with a diffractometer equipped with Cu-Kα radiation (λ = 0.15406 nm, D8FOCUS, Bruker) was used to study the crystallographic information of the samples. Diffractograms were collected in the 2θ range between 10° and 80° in 0.1° steps. Phase identification was performed by comparison with the JCPDS database. The

crystallite sizes and average crystallite sizes were determined from XRD data using Scherrer's equation (S1):

$$D = \frac{K\lambda}{\beta\cos\theta}\#(S1)$$

, where K is the Scherrer constant with a value of 0.9, λ is determined by wavelength of the X-ray sources with a value of 0.15406 nm, β and θ are the full width at half maxima (FWHM) and position of the XRD diffraction peak, respectively.

Specific surface area (S_{BET}) information was obtained by N_2 sorption isotherm using a Quanta Chrome Autosorb IQ analyzer at liquid N_2 temperature (-196 °C). Prior to analysis, the samples were outgassed at 300 °C under vacuum for 10 h. The Brunauer-Emmett-Teller (BET) surface area was calculated using experimental points at a relative pressure of $P/P_0 = 0.05\sim0.35$.

Temperature programmed reduction by H_2 (TPR) was described as follow: H_2 consumption was recorded online together with heating temperature by a thermal conductivity detector (TCD, Huasi, China) and the TCDs were collected from 100 °C to 600 °C in a nitrogen stream. After cooling in nitrogen to 100°C, a 5% H_2/N_2 flow of 30 mL/min was introduced through a quartz reactor containing the sample (100 mg). Temperature-programmed desorption of O_2 (O_2-TPD) was also analyzed with an online mass spectrometer. O_2 concentrations were determined with m/z=32. For the O_2-TPD, 0.1 g of catalyst was pretreated with Ar at 200 °C for 30 min and then 10% O_2/Ar was introduced onto the catalyst surface at 100 °C for 60 min. Next, the sample was purged with Ar for 1 h to remove externally adsorbed molecular oxygen, the catalyst was cooled to ambient temperature, and the microreactor was heated from ambient to 650 °C under Ar flow at a heating rate of 5 °C·min^{-1}. Before measurement, samples were degassed under flowing nitrogen (30 mL/min) at 300°C for 1 h.

The morphology was carried out on the SU-8010 scanning electron microscope (SEM) of Hitachi (Japan), and the electrically conductive sample was processed by a surface spray of about 1 min. Besides, a JEM-2100 (Jeol, Japan) high-resolution transmission electron microscopy (HRTEM) was also employed to observe the crystal lattice fringe and internal microstructure (the operating voltage is 200 kV). X-ray

photoelectron spectroscopy (XPS) instrument (Shimadzu, Japan) equipped with a monochromatic Mg/Al Kα was used to analyze the superficial layer properties. The binding energy was calibrated by the C 1s peak (B.E. = 284.8 eV) as a reference. The surface composition and chemical state were determined according to the position and areas of binding energies of Mn 2p, Mn 3s and O 1s peaks.

This experiment employs an oxygen isotope device comprising a vacuum pump, a circulation pump, a heating furnace, a U-shaped micro-reaction tube (volume 70 cm³) and numerous gas pipelines. The signals of reactants are recorded by mass spectrometry (OmniStar, Germany). The 100 mg sample was subjected to a pre-treatment process in an oxygen-enriched atmosphere where it was heated to a temperature of 300 °C. Excess $^{16}O_2$ was removed under dynamic vacuum conditions for 30 minutes after the temperature reached 200°C. Subsequently, an oxygen isotope ($^{18}O_2$) was introduced into the reaction system for OIE reaction, at a pressure of 65.0 ± 1.5 mbar. The catalyst was then heated to 600°C, and the mass spectrometer was simultaneously activated.

The mass spectrometer was used to record changes in concentration of the following isotopes: $^{18}O_2$ (P36), $^{16}O_2$ (P32), and $^{16}O^{18}O$ (P34). These isotopes were selected for analysis due to their potential role in oxygen exchange reactions. Moreover, N2 (m/z=28) was recorded to ascertain whether there were any leaks in the vacuum system. Figure S1 illustrates the configuration of an apparatus designed for the isotopic exchange of oxygen.
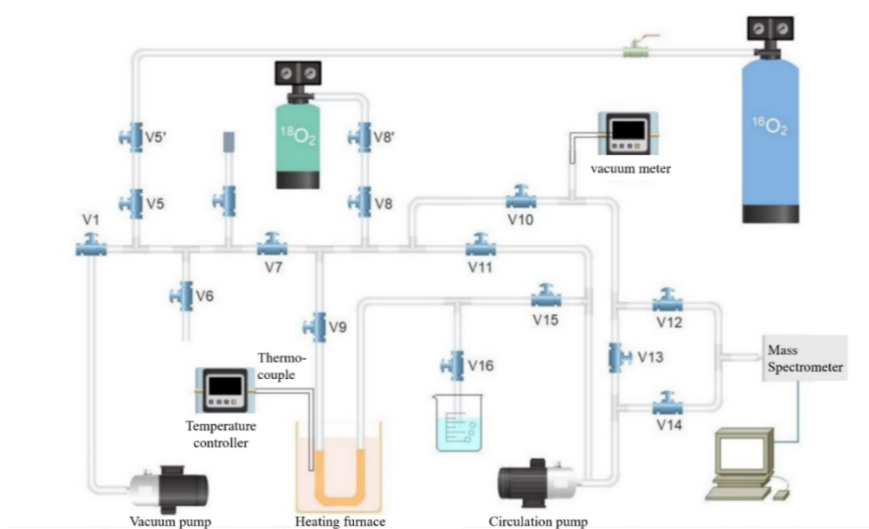

Figure S2 Schematic diagram of the oxygen isotopic exchange experiment

According to Royer[S2] and Martin[S3], the rate of exchange (Re, atom/(g·s)) is

calculated from the rate of disappearance of ^{18}O from the phase gas at time t:

$$R_e = -2N_g \cdot \frac{d\alpha_g^t}{dt} = 2N_s \cdot \frac{d\alpha_s^t}{dt} \#(S2)$$

where N_g and N_s are respectively the total number of oxygen atoms in gas phase and the number of exchangeable oxygen atoms at the oxide surface.

α_g^t and α_s^t are the ^{18}O atomic fraction in the gas phase and the ^{18}O atomic fraction at the surface at each time.

α_g^t is calculated from the partial pressure of $^{18}O_2$, $^{16}O_2$ and $^{16}O^{18}O$ at each time:

$$\alpha_g^t = \frac{\frac{1}{2} \cdot P_{34}^t + P_{36}^t}{P_{32}^t + P_{34}^t + P_{36}^t} \#(S3)$$

and N_g is obtained as follows:

$$N_g = \frac{N_A P_t}{R}\left(\frac{V_r}{T_r} + \frac{V_c}{T_c}\right) \#(S4)$$

where N_A is Avogadro's number, P_T is total pressure, R is the gas constant, V_r and V_c are the volumes of the heated and nonheated parts of the system, T_r and T_c are the temperatures of the heated and nonheated parts of the system.

In the test conditions, the initial rate of exchange was calculated from the initial slopes with respect to time of the partial pressure of $^{18}O_2$ ($\frac{dP_{36}^0}{dt}$) and $^{16}O^{18}O$ ($\frac{dP_{34}^0}{dt}$):

$$R_e = -\frac{N_A}{R}\left(\frac{V_r}{T_r} + \frac{V_c}{T_c}\right)\left(2\frac{dP_{36}^0}{dt} + \frac{dP_{34}^0}{dt}\right) \#(S5)$$

The number of exchanged atoms at each time is calculated from the number of ^{18}O atoms at time t:

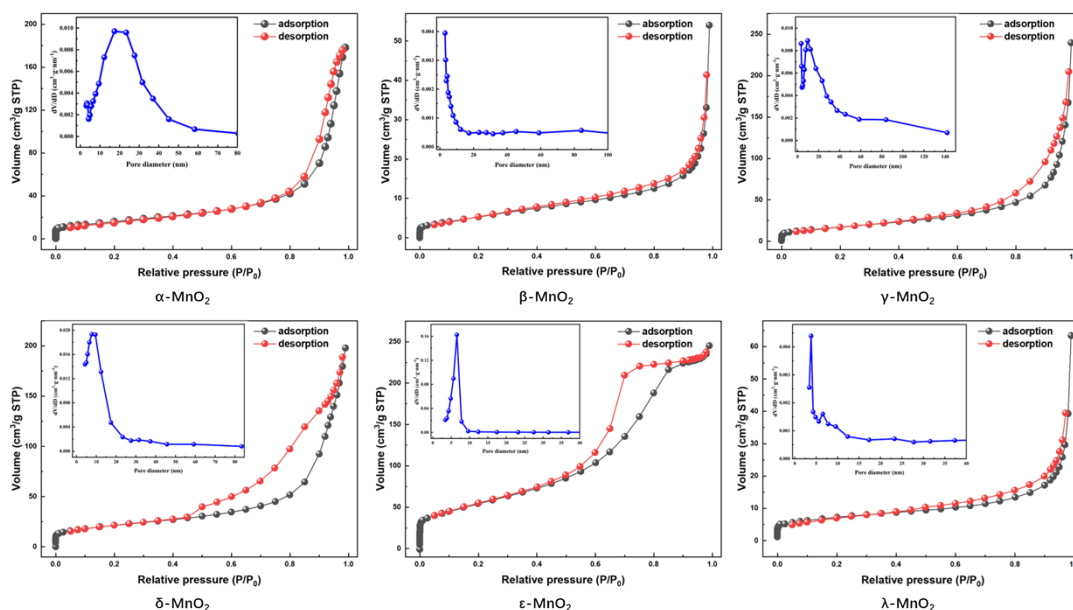$$N_e^t = \left(\alpha_g^0 - \alpha_g^t\right)N_g \#(S6),,$$

Figure S3 The nitrogen adsorption–desorption isotherms of MnO_2 samples

As can be seen from the SEM figures, the structures of α-MnO_2 (Figure S4 a), β-MnO_2 (Figure S4 b), and γ-MnO_2 (Figure S4 c) are relatively similar and all of them are spheres composed of fiber rods with diverse lengths, which is because they belong to the same one-dimensional MnO_2 structure. While δ-MnO_2 (Figure S4 d) and ε-MnO_2 (Figure S4 e) are spheres compose of petal like flakes or thicker plates, which is due to the fact that δ-MnO_2 and ε-MnO_2 belong to a two-dimensional lamellar structure. In contrast, λ-MnO_2 is an irregular three-dimensional structure formed by the cross-stacking of small discs. The difference between α-MnO_2, β-MnO_2, and γ-MnO_2 is that the spheres of β-MnO_2 (10-15 μm) exhibit a relatively large size, whereas those of α-MnO_2 and γ-MnO_2 (4-6 μm) display a relatively reduced diameter. Besides, the α-MnO_2 and γ-MnO_2 are comprised by nanorods with the diameter of 20-80 nm and 10-15 nm, while β-MnO_2 is composed of rods with large diameters of 100-150 nm and lengths of 100 nm and 1.5 μm. Generally, among these one-dimensional MnO_2, higher specific surface area is essentially correlated with smaller diameter of primary rods and size of secondary constructed sphere. Moreover, the petal-like units comprising δ-MnO_2 have diameters in the range of 150-200 nm and thicknesses in the range of 10 nm. Whereas the plates constituting ε-MnO_2 have thickness of about 60 nm. The secondary constructure of λ-MnO_2 has a diameter in the range of 150-350 nm and a thickness of approximately 30 nm.
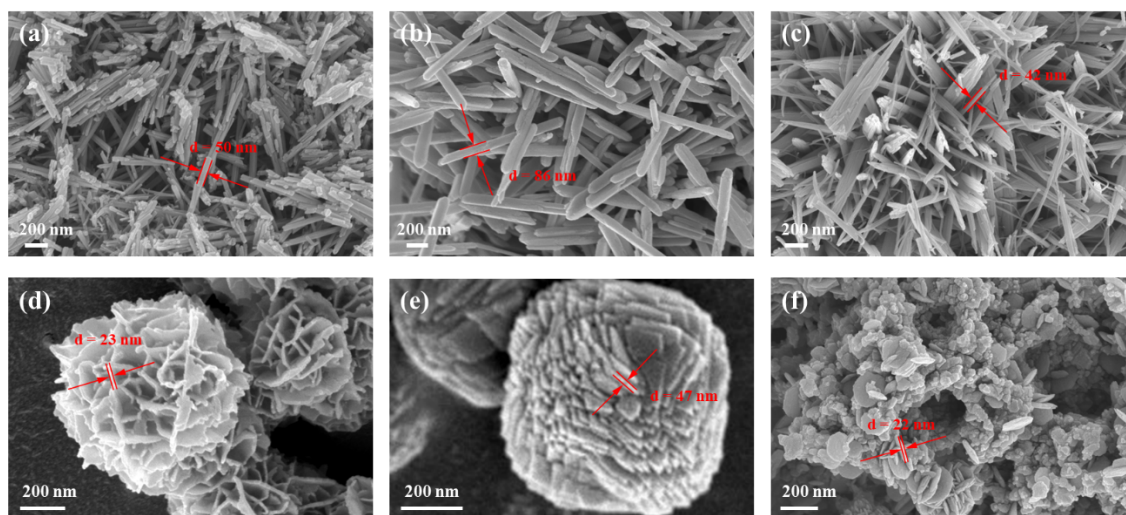
Figure S4 The SEM images and the sizes of (a) α-MnO$_2$, (b) β-MnO$_2$, (c) γ-MnO$_2$, (d) δ-MnO$_2$, (e) ε-MnO$_2$ and (f) λ-MnO$_2$.
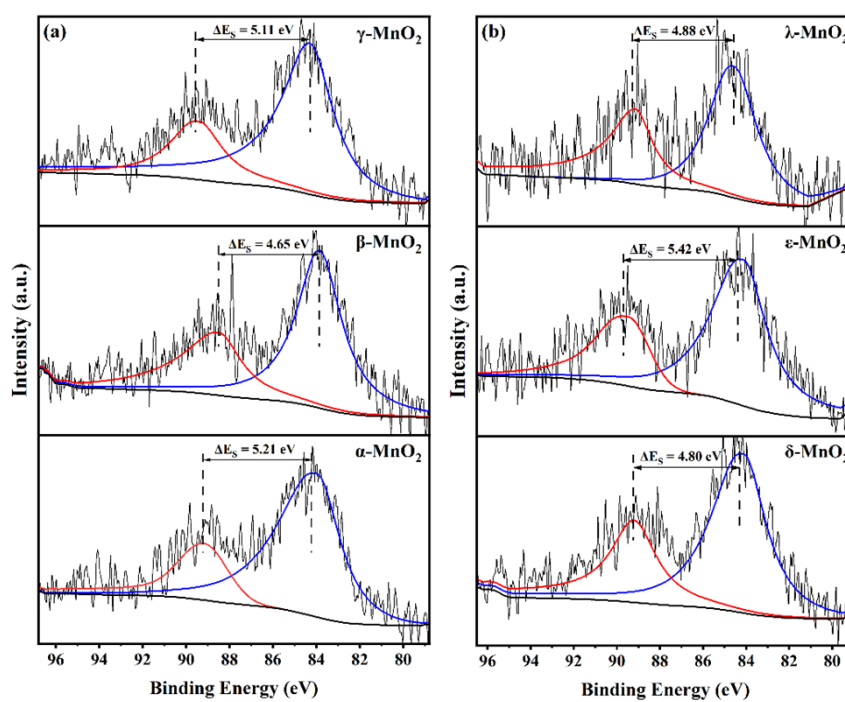

Figure S5 Mn3s XPS spectra of MnO$_2$

Table S1 Quantitative results on Raman mapping of MnO$_2$

	Peak center	FWHM	Peak area
α-MnO$_2$	635.1	51.17	3319
β-MnO$_2$	632.1	51.89	9819
γ-MnO$_2$	638.1	52.29	3986

δ-MnO$_2$	629.0	22.01	19824
ε-MnO$_2$	635.1	77.00	2789
λ-MnO$_2$	635.1	47.29	8051

Table S2 Quantitative analysis of O$_2$-TPD

	β-O$_2$ (°C)	Area (×10^{-7})
α-MnO$_2$	548	6.49
β-MnO$_2$	679	2.94
γ-MnO$_2$	543	3.15
δ-MnO$_2$	604	3.60
ε-MnO$_2$	501	6.86
λ-MnO$_2$	596	1.94

In order to ensure the validity of the structures, the iodometric titration was used to check average oxidation state of the accurate bulk manganese. The details are as follow:

Prepare KI solution and starch solution with a mass concentration of 0.5%, add 0.0625 g of MnO$_2$ to 50 ml of KI solution, then add an excess of diluted HCl, leave it in the dark and react for 20 min. Then add a few drops of starch solution, titrate with Na$_2$S$_2$O$_3$ until the solution becomes transparent. The reaction equation is as follows:
$$MnO_2 + 4HCl + 2KI \rightarrow MnCl_2 + I_2 + 2H_2O$$
$$I_2 + 2Na_2S_2O_3 \rightarrow 2NaI + Na_2S_4O_6$$
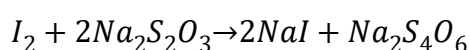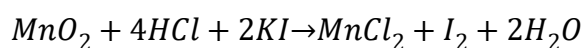
According to the consumption of Na$_2$S$_2$O$_3$, we can calculate the average oxidation state of the bulk MnO$_2$.

Table S3 Results of iodometric titration

Catalyst	Na$_2$S$_2$O$_3$ consumed (mL)	AOS	AOS by Mn3s	The content of surface/bulk Mn^{3+}
α-MnO$_2$	12.19	3.25	3.09	95.08
β-MnO$_2$	14.67	3.91	3.72	95.14
γ-MnO$_2$	12.51	3.34	3.2	95.81
δ-MnO$_2$	13.89	3.7	3.55	95.94

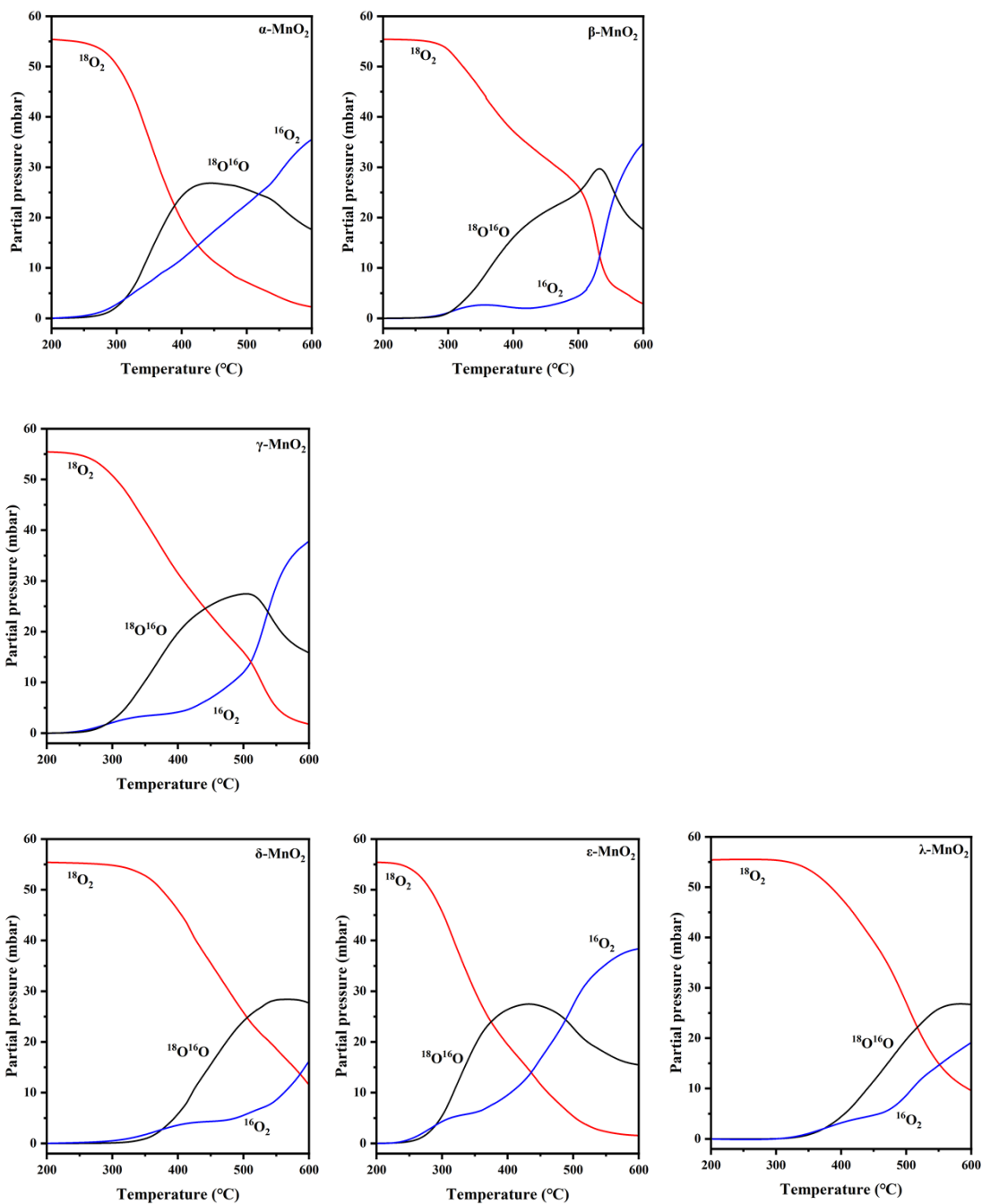|				
ε-MnO$_2$	12.1	3.23	2.85	88.24
λ-MnO$_2$	13.12	3.5	3.46	98.86
MnO$_2$ (Theoretical)	15	4		

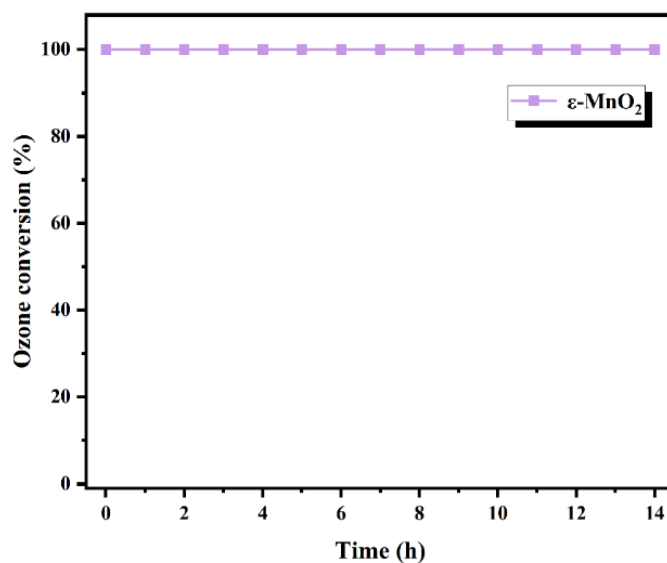Figure S6 Temperature programmed reaction of the $^{18}O_2/^{16}O_2$ isotopic exchange of MnO$_2$ samples

Figure S7 Stability test of ε-MnO$_2$

Table S4 Comparison of the activity of related Mn-based catalysts

Catalyst	Reaction condition	Activity remained after 120 min	Reference
MnCuNiO$_x$	GHSV = 63700 h^{-1}, 2 ppm O$_3$, 25 °C, dry air	73%	Chernykh [S17]
CeFeMnO$_x$	WHSV = 1200 L·g^{-1}·h^{-1}, 130 ppm O$_3$, 25 °C, dry air	86%	Chen et.al [S18]
Fe-OMS-2	GHSV = 336000 h^{-1}, 50 ppm O$_3$, 30 °C, dry air	93%	Qiang et.al [S19]
Pd-MnO$_x$ /SiO$_2$	GHSV = 380000 h^{-1}, 0.6 ppm O$_3$, 14 °C, RH = 85-90 %	82%	Ren et.al [S20]
ε-MnO$_2$	WHSV = 300 L·g^{-1}·h^{-1}, 40 ppm O$_3$, 25 °C, dry air	100%	This study

S2. Computation section

2.1 Computation details

Density functional theory (DFT) calculations were carried out to investigate the

characteristics of MnO_2 crystals as well as ozone decomposition behaviors occurring over them using the Perdew–Burke–Ernzerhof functional and projector-augmented wave pseudopotentials in the Vienna Ab initio Simulation Package[S4, S5]. The projected augmented wave (PAW)[S6] pseudopotential was used to explain the interaction between core electrons and valence electrons. The calculation of the electronic exchange correlation functions was performed using the generalized gradient approximation (GGA) of Perdew–Burke–Ernzerhof with Hubbard U corrections (PBE + U)[S7-S9]. The PBE + U method with a Ueff value for Mn $3d$ orbitals (U-J = 3.9 eV) was applied to correctly predict the ground-state electronic properties of Mn in various MnO_2 cells[S10, S11]. The transition states (TS) were obtained by employing the nudged elastic band (NEB) method[S12, S13]. All slab calculations were performed using a Monkhorst–Pack grid (K-Mesh = 0.030) with a cutoff energy of 500 eV and the smearing parameter set to 0.02 eV. The constraint value was set to 1×10^{-5} energy charge between two consecutive iterations to achieve SCF convergence. A spin polarization is applied, initializing magnetic moments to 5 µB for transition metals[S14, S15].
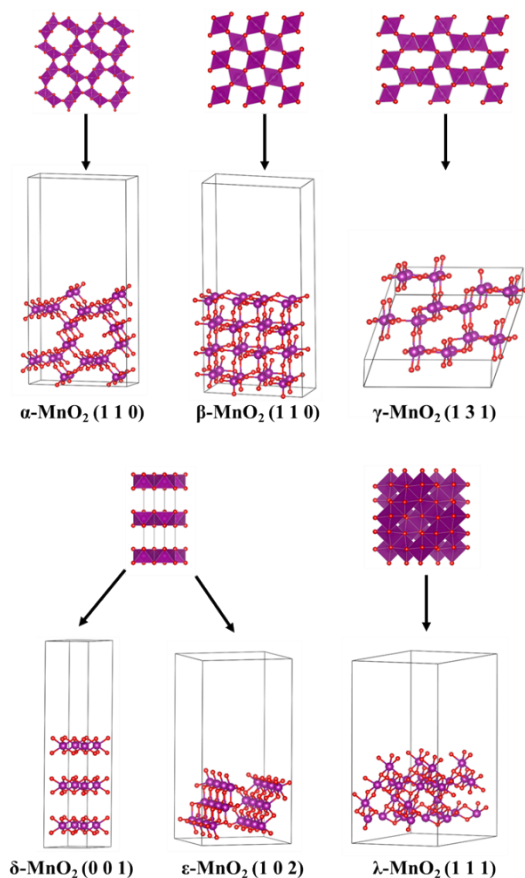

α-MnO_2 (1 1 0)   β-MnO_2 (1 1 0)   γ-MnO_2 (1 3 1)

δ-MnO_2 (0 0 1)   ε-MnO_2 (1 0 2)   λ-MnO_2 (1 1 1)

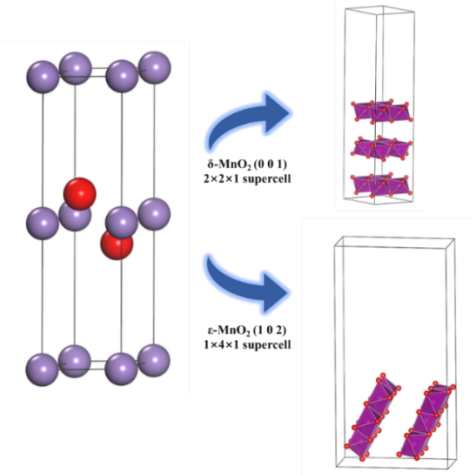Figure S8 unit cell and respective exposed surface models of MnO$_2$

Figure S9 unit cell and supercell models of δ-MnO$_2$ and ε-MnO$_2$

In order to eliminate the influence of specific surface area[S16], the normalized reaction rate (R_{norm}, mol·m^{-2}·s^{-1}) is derived from formula S1. Where C_{in} (mol·s^{-1}) is the concentration of ozone in inlet gas, F (mol·s^{-1}) is the ozone flow rate, m_{cat} (g) is the mass of catalyst, S_{BET} (m^2·g^{-1}) is the specific surface area, X_{ozone} is the ozone conversion.

$$R_{norm} = \frac{C_{in} \cdot F}{m_{cat} \cdot S_{BET}} \cdot ln(\frac{1}{1 - X_{ozone}}) \#(S7)$$
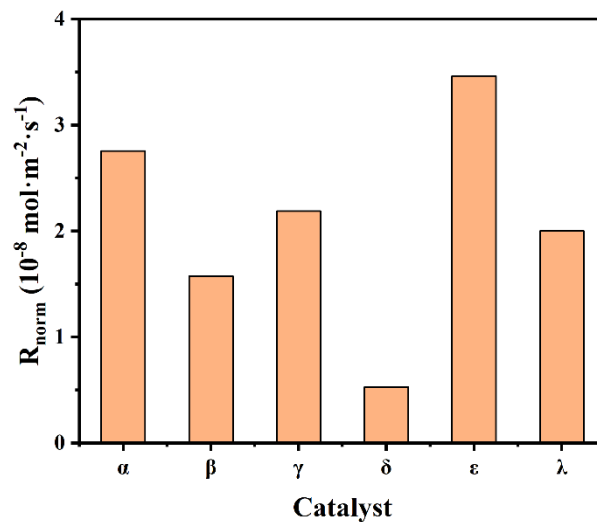

Figure S10 The normalized reaction rate of MnO$_2$ samples

S3. References

S1.   T. Hatakeyama, N. L. Okamoto and T. Ichitsubo, Thermal stability of MnO2 polymorphs, *Journal of Solid State Chemistry*, 2022, **305**, 122683.

S2.   D. Martin and D. Duprez, Mobility of Surface Species on Oxides. 1. Isotopic Exchange of $^{18}O_2$ with ^{16}O of SiO_2, Al_2O_3, ZrO_2, MgO, CeO_2, and CeO_2-Al_2O_3. Activation by Noble Metals. Correlation with Oxide Basicity**,** *J. Phys. Chem.*, 1996, 100, 9429-9438.

S3.   S. Royer, D. Duprez and S. Kaliaguine, Role of bulk and grain boundary oxygen mobility in the catalytic oxidation activity of $LaCo_{1-x}Fe_xO_3$, *J. Catal.*, 2005, **234**, 364-375.

S4.   G. Kresse and J. Furthmüller, Efficient iterative schemes for ab initio total-energy calculations using a plane-wave basis set, *Physical Review B*, 1996, **54**, 11169-11186.

S5.   V. Wang, N. Xu, J.-C. Liu, G. Tang and W.-T. Geng, VASPKIT: A user-friendly interface facilitating high-throughput computing and analysis using VASP code, *Computer Physics Communications*, 2021, **267**, 108033.

S6.   G. Kresse and D. Joubert, From ultrasoft pseudopotentials to the projector augmented-wave method, *Physical Review B*, 1999, **59**, 1758-1775.

S7.   J. P. Perdew, K. Burke and M. Ernzerhof, Generalized Gradient Approximation Made Simple, *Physical Review Letters*, 1996, **77**, 3865-3868.

S8.   M. An, H.-M. Zhang, Y.-K. Weng, Y. Zhang and S. Dong, Possible ferrimagnetism and ferroelectricity of half-substituted rare-earth titanate: A first-principles study on Y0.5La0.5TiO3, *Frontiers of Physics*, 2015, **11**, 117501.

S9.   D. Wines, K. Saritas and C. Ataca, Intrinsic Ferromagnetism of Two-Dimensional (2D) MnO2 Revisited: A Many-Body Quantum Monte Carlo and DFT+U Study, *The Journal of Physical Chemistry C*, 2022, **126**, 5813-5821.

S10.   A. Jain, G. Hautier, C. J. Moore, S. Ping Ong, C. C. Fischer, T. Mueller, K. A. Persson and G. Ceder, A high-throughput infrastructure for density functional theory calculations, *Computational Materials Science*, 2011, **50**, 2295-2310.

S11. C. Ling and F. Mizuno, Capture Lithium in αMnO2: Insights from First Principles, *Chemistry of Materials*, 2012, **24**, 3943-3951.

S12. D. H. Mathews and D. A. Case, Nudged Elastic Band Calculation of Minimal Energy Paths for the Conformational Change of a GG Non-canonical Pair, *Journal of Molecular Biology*, 2006, **357**, 1683-1693.

S13. D. Sheppard, R. Terrell and G. Henkelman, Optimization methods for finding minimum energy paths, *The Journal of Chemical Physics*, 2008, **128**, 134106.

S14. Y.-F. Li, S.-C. Zhu and Z.-P. Liu, Reaction Network of Layer-to-Tunnel Transition of MnO2, *Journal of the American Chemical Society*, 2016, **138**, 5371-5379.

S15. W. Zhong, Y. Qiu, H. Shen, X. Wang, J. Yuan, C. Jia, S. Bi and J. Jiang, Electronic Spin Moment As a Catalytic Descriptor for Fe Single-Atom Catalysts Supported on C2N, *Journal of the American Chemical Society*, 2021, **143**, 4405-4413.

S16. F. Wang, H. Dai, J. Deng, G. Bai, K. Ji and Y. Liu, Manganese Oxides with Rod-, Wire-, Tube-, and Flower-Like Morphologies: Highly Effective Catalysts for the Removal of Toluene, *Environmental Science & Technology*, 2012, **46**, 4034-4041.